

## APPLIED PHYSICS

Gate-controlled VO<sub>2</sub> phase transition for high-performance smart windowsShi Chen<sup>1\*</sup>, Zhaowu Wang<sup>2,3\*</sup>, Hui Ren<sup>1</sup>, Yuliang Chen<sup>1</sup>, Wensheng Yan<sup>1</sup>, Chengming Wang<sup>2</sup>, Bowen Li<sup>1</sup>, Jun Jiang<sup>2†</sup>, Chongwen Zou<sup>1†</sup>

Vanadium dioxide (VO<sub>2</sub>) is a promising material for developing energy-saving “smart windows,” owing to its infrared thermochromism induced by metal-insulator transition (MIT). However, its practical application is greatly limited by its relatively high critical temperature (~68°C), low luminous transmittance (<60%), and poor solar energy regulation ability (<15%). Here, we developed a reversible and nonvolatile electric field control of the MIT of a monoclinic VO<sub>2</sub> film. With a solid electrolyte layer assisting gating treatment, we modulated the insertion/extraction of hydrogen into/from the VO<sub>2</sub> lattice at room temperature, causing tristate phase transitions that enable control of light transmittance. The dramatic increase in visible/infrared transmittance due to the phase transition from the metallic (lightly H-doped) to the insulating (heavily H-doped) phase results in an increased solar energy regulation ability up to 26.5%, while maintaining 70.8% visible luminous transmittance. These results break all previous records and exceed the theoretical limit for traditional VO<sub>2</sub> smart windows, making them ready for energy-saving utilization.

## INTRODUCTION

Designing improved energy-saving materials is an active research topic in materials science because of the increasing concerns related to energy consumption and sustainable development. It is known that residential buildings are responsible for almost 30 to 40% of the primary energy consumption in the world (1). Thus, the use of chromogenic materials on building fenestration and the applications of building-integrated photovoltaic technologies such as solar cells have been demonstrated to be effective ways to increase the energy efficiency of buildings and reduce the energy consumption (2–7). Notably, smart coatings based on thermochromic materials, the so-called “smart windows,” can modulate the transmittance of solar radiation in response to the change of temperature, making them very promising for improving the energy utilization efficiency of buildings (8).

As a typical thermochromic material, vanadium dioxide (VO<sub>2</sub>) has been widely investigated because of its pronounced metal-insulator transition (MIT) behavior at the critical temperature of 68°C (9–11). During the MIT process, VO<sub>2</sub> shows a sharp change of resistance and a pronounced optical switching behavior especially in the infrared region, which makes it promising for energy-efficient coating applications (12–21). However, obstacles including high transition temperature at ~68°C, low luminous transmittance ( $T_{\text{lum}} < 60\%$ ), and weak solar energy regulation ability ( $\Delta T_{\text{sol}}$ , usually <15%), make the VO<sub>2</sub>-based smart window still far from practical (22–24).

In this study, we developed an electrochromic smart window system based on a VO<sub>2</sub> film with gate voltage control via a solid electrolyte. By adding gating voltage to control the H-doping level, we tuned non-destructive and reversible phase transformations between the insulating pristine monoclinic VO<sub>2</sub>, metallic H<sub>x</sub>VO<sub>2</sub> (0 < x < 1), and insulating

HVO<sub>2</sub> phases at room temperature. Synchrotron-based spectroscopies were used to identify the crystal structures, electronic states, and the orbital occupancies during these field-controlled phase transitions. By analyzing the optical transmission properties of this system, we have demonstrated that the solar energy regulation ability is greatly augmented ( $\Delta T_{\text{sol}} \sim 26.5\%$ ), via the transition between the metallic H<sub>x</sub>VO<sub>2</sub> (0 < x < 1) phase, which can block most infrared transmissions, and the insulating HVO<sub>2</sub> substantially, which has a high visible luminous transmittance ( $T_{\text{lum}}$  up to ~70.8%). This not only substantially surpasses the performance of systems reported previously but also exceeds the theoretical limit of  $\Delta T_{\text{sol}} \sim 23\%$  for a pure VO<sub>2</sub> material. Thus, the current results will provide a promising basis for the development of practical energy-saving devices in the future.

## RESULTS

Gating-induced reversible three-phase transitions for VO<sub>2</sub> films

An electric field applied with ion liquid (IL) gating is effective in modulating the properties of metal oxide materials. Recent reports showed that gating voltage with water-involved IL could induce the insertion/extraction of either oxygen anions or hydrogen cations into/from some oxides, implying phase modulation through electric field control (25–30). Here, we adopted a gel-like solid electrolyte [NaClO<sub>4</sub> dissolved in polyethylene oxide (PEO) matrix; see Materials and Methods] as the gating layer (Fig. 1, A and B). The solid electrolyte covered both the prepared 30-nm VO<sub>2</sub>/Al<sub>2</sub>O<sub>3</sub>(0001) thin film and the three gold electrodes. In addition, the source and drain electrodes had good contact with the VO<sub>2</sub> thin film, realizing a typical field-effect transistor (FET) configuration. Positive or negative voltages applied through the gating electrode could drive the insertion/extraction of hydrogen ions into/from the VO<sub>2</sub> lattice (29–31), resulting in the stabilization of the metallic VO<sub>2</sub> phase at room temperature due to hydrogen insertion.

Hydrogen doping in the VO<sub>2</sub> crystal was frequently studied under the high-temperature annealing treatment assisted by a noble metal catalyst in H<sub>2</sub> gas (32–34), which could also lead to the formation of a metallic H-doped VO<sub>2</sub> state. Conversely, as reported recently by Yoon *et al.* (35) and our group (36), catalyst-assisted

<sup>1</sup>National Synchrotron Radiation Laboratory, University of Science and Technology of China, Hefei 230029, China. <sup>2</sup>Hefei National Laboratory for Physical Sciences at the Microscale, CAS Center for Excellence in Nanoscience, CAS Key Laboratory of Mechanical Behavior and Design of Materials, School of Chemistry and Materials Science, University of Science and Technology of China, Hefei, Anhui 230026, China. <sup>3</sup>School of Physics and Engineering, Henan University of Science and Technology, Henan Key Laboratory of Photoelectric Energy Storage Materials and Applications, Luoyang, Henan 471023, China.

\*These authors contributed equally to this work.

†Corresponding author. Email: jiangj1@ustc.edu.cn (JJ.); czou@ustc.edu.cn (C.Z.)

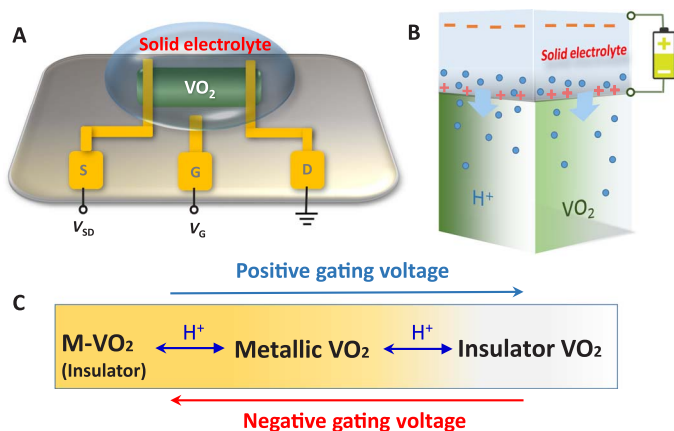


**Fig. 1. Experimental schemes.** (A) The gating diagram of the VO<sub>2</sub> device with source, drain, and gate electrodes. (B) Hydrogen ion movement under gating control. (C) The reversible insulator-metal-insulator tristate phase transitions of VO<sub>2</sub> by tuning hydrogenating level with positive (blue) or negative (red) gating voltages.

high-temperature annealing can produce another insulating HVO<sub>2</sub> phase. Thus, is it possible to realize the tristate phase transitions as shown in Fig. 1C by the gating treatment at room temperature?

As expected, phase transitions are found to be strongly dependent on the gating voltage. Figure 2A shows the changes in electrical resistance under gating voltages of 1.0 and 2.0 V, respectively, as a monitor of the phase transitions between insulator and metallic states (see the laboratory-scale gating device in fig. S1A). At a gating voltage of 1.0 V, the film resistance gradually decreases from  $\sim 10^6$  to  $\sim 10^3$  ohms even after 400 min (red curve), indicating a transition from an insulator to a metallic state. Upon the application of a gating voltage of 2.0 V (green curve), the film resistance first decreases from  $\sim 10^6$  to  $\sim 3 \times 10^3$  ohms after about 25 min and then gradually increases up to  $\sim 2 \times 10^5$  ohms, indicating a transition from an insulator to a metallic state, and then back to an insulator state. This gating process is also sensitive to sample temperature (see fig. S1B): The higher the temperature, the quicker the gating-induced phase changes appear. For example, at 60°C, the gating-induced phase transition can be finished within several minutes, which demonstrates the potential for fast switching during practical applications. Figure 2B shows the x-ray diffraction (XRD) measurements for the pristine VO<sub>2</sub> film and the samples gated by 1.0- or 2.0-V gating for 300 min, respectively. In contrast to the 39.8° XRD peak of the VO<sub>2</sub> (020) diffraction for the nongated pristine sample, peaks at 39.4° and 36.8° are assigned to the gating-induced metallic film and the insulating sample by 1.0 and 2.0 V, respectively (36). One can also monitor the varying of XRD signals (Fig. 2C) to understand the gradual evolution of crystal structures during the gating cycles. It is observed that the reversible phase modulations are made by adjusting voltages as a function of gating time (Fig. 2D). Starting from the pristine VO<sub>2</sub> structure, the original insulating sample is first transformed to the metallic phase by a gating voltage of 1.0 or 1.5 V. A new insulating phase is formed when the gating voltage is increased to 2.0 V. Then, upon the addition of a negative voltage of  $-1.0$  V, the insulating VO<sub>2</sub> is gradually converted to the metallic phase. The initial monoclinic VO<sub>2</sub> phase is recovered by further increasing the negative voltage to  $-2.0$  V.

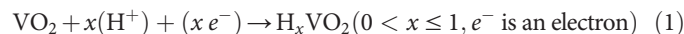
Loop tests were conducted by keeping the source-drain voltage of 0.3 V while sweeping the gating voltage at either a fast or a slow rate. Under the fast sweeping mode with a rate of 0.4 mV/s (Fig. 2E), the

film resistance gradually decreased from  $\sim 10^6$  to  $\sim 10^3$  ohms as the gating voltage increased from 0.0 to 2.0 V (starting from point A), indicating a transition from an insulator to a metallic state. If the voltage decreased from 2.0 to  $-2.0$  V, the metallic state ( $\sim 10^3$  ohms) was maintained, but once the negative gating voltage reached a threshold value, it completely changed to an insulator state ( $\sim 10^6$  ohms). Thus, during the fast-rate loop test, a simple and reversible transition between the insulator M-VO<sub>2</sub> and the metallic H<sub>x</sub>VO<sub>2</sub> state was observed. Conversely, when applying the gating voltage at a slower sweeping rate of 0.1 mV/s, a quite different variation contour involving tristate phase transitions was obtained (Fig. 2F). Along the positive gating direction, the film was transformed from the initial M-VO<sub>2</sub> state (point A) to the metallic H<sub>x</sub>VO<sub>2</sub> state (point B), and then higher positive voltage led to another insulating HVO<sub>2</sub> state (point C). Thereafter, as the gating voltage decreased toward  $-2.0$  V, the insulating HVO<sub>2</sub> phase was first changed back to the metallic state and then eventually reverted to the initial insulating M-VO<sub>2</sub> state, finishing a full cycle. This transition loop was ascribed to the sequential insulator-metal-insulator tristate phase transitions. This was consistent with the resistance varying as a function of gating time in Fig. 2A, as the 2.0-V gating treatment gradually turned the pristine structure to the metallic state and later to the insulating phase. Accordingly, for gating treatment, both the gating voltage and gating time were key factors for phase modulation as they are the primary determinants of the degree of hydrogen insertion and diffusion into the VO<sub>2</sub> lattice.

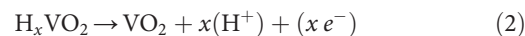
### Gating-induced hydrogen doping in VO<sub>2</sub> films

We then performed additional experiments to identify the varying of the VO<sub>2</sub> crystal structure along with gating treatment. By gating with positive voltage, the cations will be driven into the VO<sub>2</sub> lattice. Since the radius of Na<sup>+</sup> ( $\sim 0.102$  nm) is a bit larger than that of V<sup>4+</sup> ( $\sim 0.058$  nm), it is quite difficult to insert Na<sup>+</sup> in the electrolyte into the VO<sub>2</sub> lattice or for it to replace other cations there. The detailed x-ray photoelectron spectroscopy (XPS) test (see fig. S2) validates the situation, while secondary ion mass spectrometry (SIMS) tests (see fig. S3) reveal that the metallic and insulating phases induced by positive gating hold increased hydrogen concentrations.

The mechanism of hydrogen doping into the VO<sub>2</sub> lattice by gating treatment basically involves the migration of hydrogen driven by the electric field, which is analogous to the charging and discharging process in a Li<sup>+</sup> battery or the catalyst-free hydrogenation of VO<sub>2</sub> in acid solution (37). The chemical reaction for the hydrogenation can be described as



In this process, (H<sup>+</sup>) migrates into VO<sub>2</sub> from the electrolyte driven by the positive gating voltage, and the electron is provided through the gating circuit. For the restoration process, the chemical reaction is



Protons will migrate into the electrolyte from the VO<sub>2</sub> lattice because of the negative gating voltage.

For this gating treatment, the source of protons in the electrolyte should be considered (25–27, 30). Our gating experiment shows that 1.0-V gating voltage can induce the metallic H-doped VO<sub>2</sub> film. As

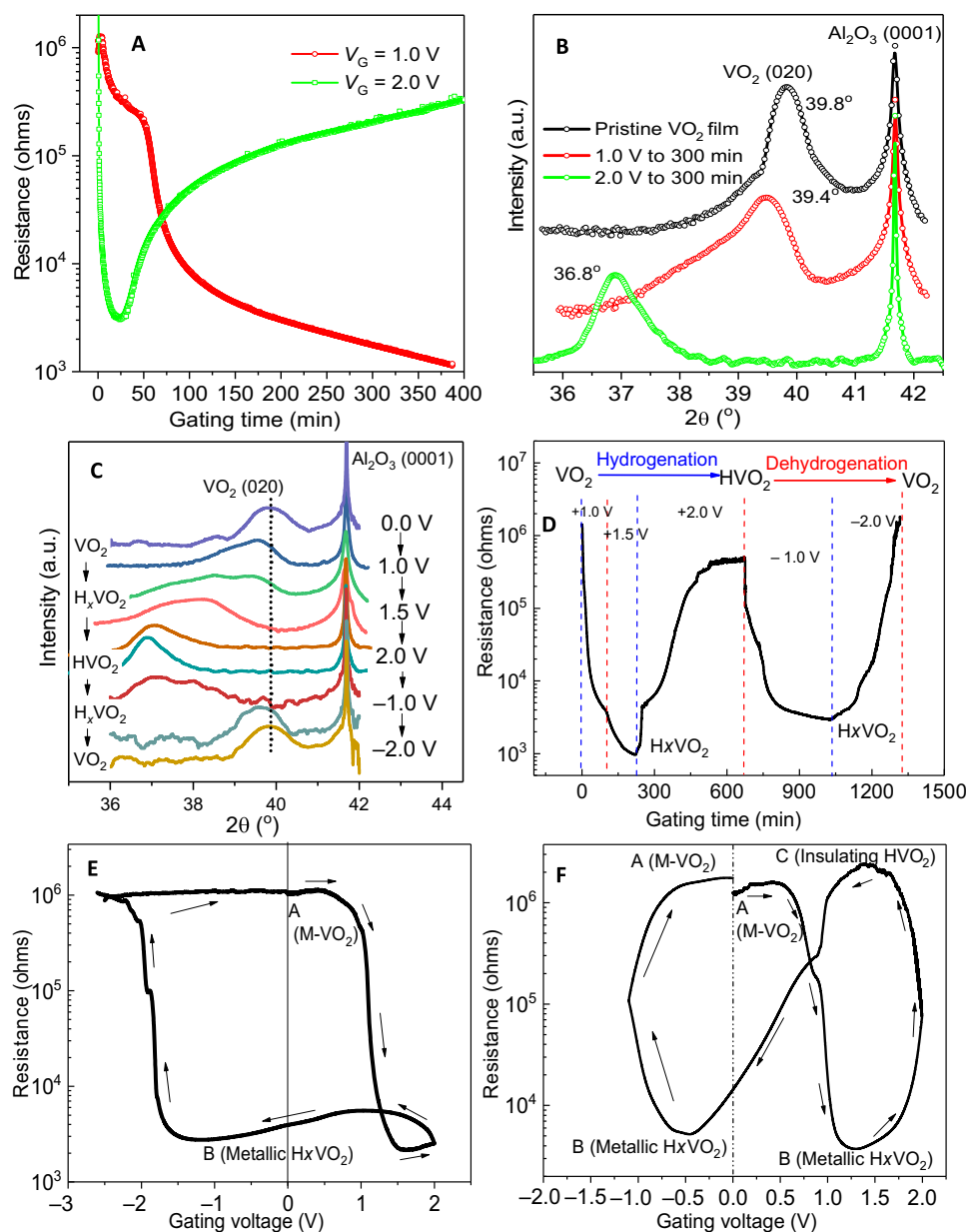


**Fig. 2. Phase modulation by the gating treatment.** (A) The resistance changes as a function of gating time at gating voltages of 1.0 V (red) or 2.0 V (green). (B) XRD curves for the pristine  $\text{VO}_2$  film (black) and for  $\text{VO}_2$  films subjected to gating voltages of 1.0 V (red) or 2.0 V (green) for 300 min. a.u., arbitrary units. (C) XRD curves for  $\text{VO}_2$  films treated with different gating voltages. To monitor the intermediate states, the gating time was set to 60 min for voltages of 1.0 and  $-2.0$  V, while it was set to 60 and 120 min for voltages of 1.5, 2.0, and  $-1.0$  V. (D) The reversible phase modulations by different voltages as a function of gating time. (E) A cycling resistance test plot produced by sweeping the gating voltage from  $-2.0$  to  $2.0$  V at a sweep rate of  $0.4$  mV/s and a source-drain voltage of  $0.3$  V, indicating a series of reversible phase transitions between the insulating monoclinic  $\text{M-VO}_2$  state (starting from point A) and the metallic  $\text{H}_x\text{VO}_2$  state. (F) A cycling resistance test plot at a slower sweep rate of  $0.1$  mV/s and a source-drain voltage of  $0.3$  V, indicating a series of reversible phase transitions between three states: the initial monoclinic insulator  $\text{M-VO}_2$  state (point A), the metallic  $\text{H}_x\text{VO}_2$  state (point B), and the insulating  $\text{HVO}_2$  state (point C). Arrows indicate the direction of resistance changes during voltage sweeping.

this voltage is less than the  $1.23$  V required for electrolysis of water, the adsorbed water in the electrolyte layer is unlikely to be the source of protons. Residual methanol in the electrolyte (see fig. S4) might be the possible source of protons because of its lower electrolysis voltage, although further chemical or electrochemical studies are required to confirm it.

In addition, it was also observed that these H-doped  $\text{VO}_2$  films were quite stable in air (see fig. S5), which demonstrated the non-

volatile property of the electric field control phase transitions under ambient conditions. Raman tests (see fig. S6) on gated samples suggested that the hydrogenated  $\text{VO}_2$  film showed a rutile-like phase structure since the characteristic peaks at  $192$ ,  $223$ , and  $617$   $\text{cm}^{-1}$  in pristine monoclinic  $\text{VO}_2$  were completely absent. These phase structures were sensitive to the H-doping concentration, providing further validation that hydrogen ions are being inserted into the  $\text{VO}_2$  lattice.

Detailed synchrotron-based XPS and x-ray absorption near-edge spectroscopy (XANES) in Fig. 3 show that pronounced peaks due to the presence of  $\text{-OH}$  emerge in the metallic phase after gating treatment at 1.0 to 1.5 V. In addition, the peak becomes much stronger with higher voltage and longer treatment time (Fig. 3A), reflecting a higher H-doping concentration in the newly formed insulating state. Specifically, the  $\text{V}2\text{p}_{3/2}$  peaks in the XPS curves become broader and slightly shift toward the low binding energy direction after gating treatment, indicating the appearance of a small amount of  $\text{V}^{3+}$  state due to the charge transfer induced by H atoms (38). Synchrotron-based XANES for V L-edge in Fig. 3B confirms the electronic structure variations induced by H-doping during the gating treatment. The V  $\text{L}_{\text{III}}$ -edge undergoes a pronounced shift to lower energy after gating, indicating that the V atoms are in a lower valence state (39, 40). The O K-edges in Fig. 3C show the transitions from  $\text{O}1\text{s}$  to  $\text{O}2\text{p}$  states, in which two distinct features of the  $t_{2g}$  and  $e_g$  peaks reflect the unoccupied states. The intensity ratio of  $t_{2g}/e_g$  decreased substantially with the gating treatment, which is caused by the increased H-doping concentration and reflects the fact that  $t_{2g}$  levels including the  $d_{ij}^*$  and  $\pi^*$  orbitals are gradually filled by electrons.

### Theoretical simulations for the gating effects

First-principles calculations at the density functional theory (DFT) level were carried out to explore the underlying microscopic mechanism of the gating effects. The formation energies of H-doping and H-diffusion energy barrier were computed using supercells containing different H concentrations:  $\text{V}_4\text{O}_8$ ,  $\text{HV}_4\text{O}_8$ , and  $\text{H}_2\text{V}_4\text{O}_8$  (Fig. 4, A to C). The formation energy of H-doping impurity is near  $-3.6$  eV, which is insensitive to H concentrations (see table S1). This is because all H impurities are stabilized at the center of lattice vacancy, forming relatively strong H–O bonds, as shown in Fig. 4 (B and C) (see also fig. S7). In contrast, the H-diffusion energy barrier becomes increasingly larger with the increase in H-doping concentration. In  $\text{VO}_2$ , the channels for H diffusion are mainly along the  $[100]$  direction because there are no V atoms or O atoms to hinder the diffusion (Fig. 4A). The calculated H-diffusion energy barrier value is 0.8 eV along the  $[100]$  direction (Fig. 4D). Conversely, the diffusion barriers in  $\text{HV}_4\text{O}_8$  and  $\text{H}_2\text{V}_4\text{O}_8$  were increased to 1.15 eV (Fig. 4E) and 1.38 eV (Fig. 4F), respectively. This increase is due to blockage of the channels for H diffusion by the intercalation of H atoms. Moreover, the geometric variations induced

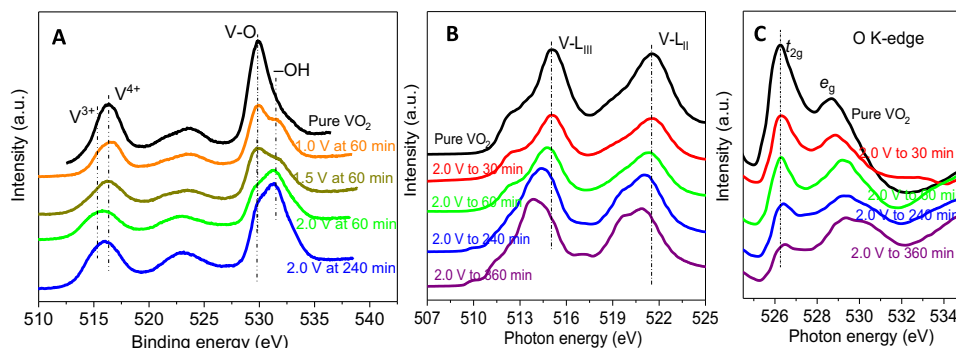


**Fig. 3. Chemical and electronic states of gating-treated  $\text{VO}_2$  films.** (A) XPS curves of  $\text{VO}_2$  films with different gating voltages. (B) V L-edge XANES curves and (C) O K-edge curves for the samples gated at 2.0 V with different gating times.

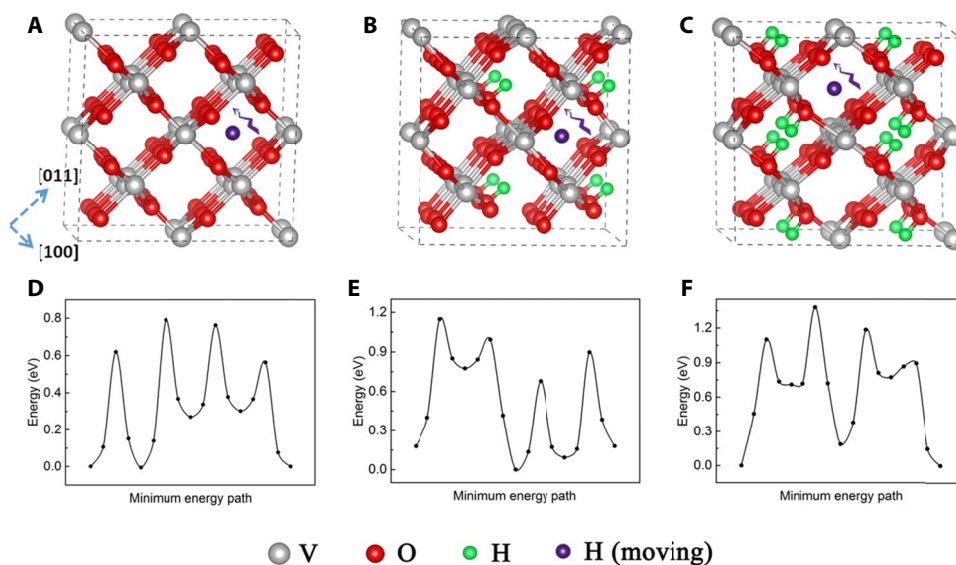


**Fig. 4. Theoretical calculation for H insertion and diffusion processes.** (A to C) Optimized atomic structures of  $\text{V}_4\text{O}_8$  (pure  $\text{VO}_2$ ),  $\text{HV}_4\text{O}_8$ , and  $\text{H}_2\text{V}_4\text{O}_8$ , respectively. Purple beads with arrows represent H-diffusion channels along the  $[100]$  direction. (D to F) Calculated energy barriers for diffusion of H atoms into  $\text{V}_4\text{O}_8$ ,  $\text{HV}_4\text{O}_8$ , and  $\text{H}_2\text{V}_4\text{O}_8$ , respectively.

by initial H-doping may also hinder the diffusion of successive H atoms. This H-dependent barrier increase explains our experimental finding that a high gating voltage of 2.0 V was required to induce the large H-doping concentration required to generate the insulation phase of the H-doped VO<sub>2</sub> film.

### Gate-controlled VO<sub>2</sub>-based smart window with high performance

The smart window concept was proposed many years ago, and many materials showed promise for use as smart windows, including hydrogels, liquid crystals, transition metal oxides, and perovskite (41, 42), because of their special optical response in the visible region upon external stimulus/excitation. The VO<sub>2</sub> material exhibited a special switching effect in the near-infrared (NIR) range across the phase transition, which demonstrated a unique advantage in energy-saving applications. Since the phase transformations of VO<sub>2</sub> films can be controlled by gating treatment at room temperature, we were able to apply it to a voltage-controlled smart window, as shown schematically in Fig. 5A. For the VO<sub>2</sub> films with three different phase structures, obvious color changes were observed. The pure VO<sub>2</sub> film and the gating-produced metallic H<sub>x</sub>VO<sub>2</sub> film showed a similar yellowish color, while the heavily H-doped VO<sub>2</sub> film was almost transparent. In Fig. 5B, the metallic H<sub>x</sub>VO<sub>2</sub> film showed transmittance spectra similar to those of the rutile VO<sub>2</sub> film (VO<sub>2</sub> film at 90°C), demonstrating a pronounced switching-off effect in the infrared region. Conversely, the insulating HVO<sub>2</sub> film maintained high transparency in both visible light and infrared regions. For example, the transmittance at 650 nm for the pristine VO<sub>2</sub> film and metallic

H<sub>x</sub>VO<sub>2</sub> was about 56%, while that of the insulating HVO<sub>2</sub> film was increased up to 72%. In the infrared region, the transmittance difference at 2000 nm for the pure VO<sub>2</sub> film across the MIT process (25° and 90°C) was about 40.3%, while the change from the metallic H<sub>x</sub>VO<sub>2</sub> film to the insulated HVO<sub>2</sub> film reached 49.1%.

On the basis of these spectral measurements, the integrated luminous transmittances (380 to 780 nm) and solar transmittances (350 to 2500 nm) can be calculated by the following equations (18)

$$T_{\text{lum}} = \int \Phi_{\text{lum}}(\lambda) T(\lambda) d\lambda / \int \Phi_{\text{lum}}(\lambda) d\lambda \quad (3)$$

$$T_{\text{sol}} = \int \Phi_{\text{sol}}(\lambda) T(\lambda) d\lambda / \int \Phi_{\text{sol}}(\lambda) d\lambda \quad (4)$$

where  $T(\lambda)$  is the transmittance function,  $\Phi_{\text{lum}}$  is equal to the standard luminous efficiency function for photopic vision, and  $\Phi_{\text{sol}}$  represents the solar irradiance spectrum for an air mass of 1.5. The solar modulation ability ( $\Delta T_{\text{sol}}$ ) of the metallic H<sub>x</sub>VO<sub>2</sub> and insulating HVO<sub>2</sub> films can be calculated by

$$\Delta T_{\text{sol}} = T_{\text{sol,insulating-HVO}_2} - T_{\text{sol,metallic-H}_{1-x}\text{VO}_2} \quad (5)$$

According to the above formula, the transparent, heavily insulating HVO<sub>2</sub> film exhibits a high  $T_{\text{lum}}$  value of about 70.8%, while the transition between the metallic and insulating phases of the H-doped VO<sub>2</sub> film is accompanied by a good  $\Delta T_{\text{sol}}$  value of 26.5% (Fig. 5C).

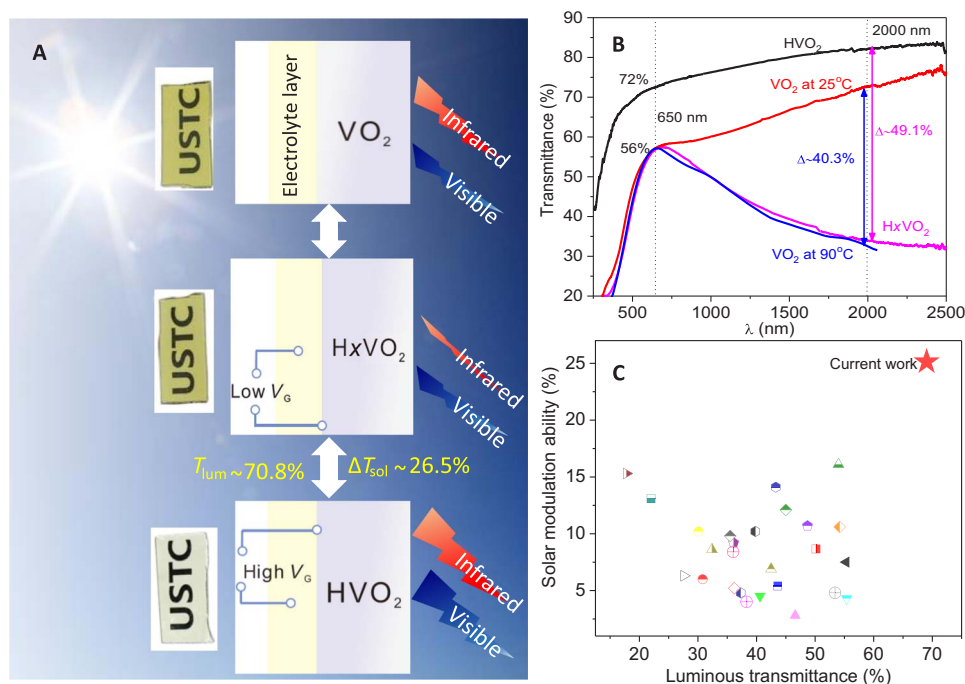


**Fig. 5. Optical properties in relation to possible smart window applications.** (A) The schematic diagram of an electrochromic smart window. Properties of three films with different phases are compared. Both the pure VO<sub>2</sub> film and the gating-produced metallic H<sub>x</sub>VO<sub>2</sub> film show a similar yellowish color, while the HVO<sub>2</sub> film is almost transparent. USTC, University of Science and Technology of China. (B) Optical transmittance spectra of VO<sub>2</sub>, H<sub>x</sub>VO<sub>2</sub>, and HVO<sub>2</sub> thin films. The transmittance at 650 nm for the pristine VO<sub>2</sub> film and metallic H<sub>x</sub>VO<sub>2</sub> is about 56%, while the insulating HVO<sub>2</sub> film has an increased transmittance of 72%. In the infrared region, the transmittance difference at 2000 nm for the pure VO<sub>2</sub> film across the MIT process (transmittance of film at 25°C compared to 90°C) is about 40.3%, while the change in transmittance from the metallic H<sub>x</sub>VO<sub>2</sub> film to the insulating HVO<sub>2</sub> film is higher at 49.1%. (C) A plot of luminous transmittance  $T_{\text{lum}}$  versus solar modulation ability  $\Delta T_{\text{sol}}$  that highlights the results of this work (★) compared to previously reported data.

The data from previous reports for traditional VO<sub>2</sub> smart windows (see table S2) are also plotted. The performance of a smart window based on the transition between the metallic and insulating phases of an H-doped VO<sub>2</sub> film appreciably surpasses previous records. Furthermore, it even surpasses the theoretical limitation of the  $\Delta T_{\text{sol}}$  of ~23% for a traditional VO<sub>2</sub> smart window, which can only be achieved by texture surface design or complex multiyear film fabrication (43).

For architectural smart coatings, the excellent luminous transmittance in the visible range and high modulation efficiency in the NIR regions are both important and greatly desirable. There are two long-lasting issues hindering the practical application of VO<sub>2</sub> in smart windows: low luminous transmittance ( $T_{\text{lum}}$ ) and poor solar energy regulation ability ( $\Delta T_{\text{sol}}$ ). For a traditional smart window constructed with the pure VO<sub>2</sub> film, increasing the VO<sub>2</sub> film thickness is necessary for better infrared switching performance, and as a result, the visible light transmittance will be greatly decreased. This problem is caused by the intrinsic band structures and optical properties of VO<sub>2</sub>, making it very difficult to be solved for the thermochromic VO<sub>2</sub> smart window. In addition, its relatively high critical temperature (~68°C) is another big obstacle for practical applications (14, 16). Thus, in this work, the voltage-controlled phase transitions between the metallic H<sub>x</sub>VO<sub>2</sub> and insulating HVO<sub>2</sub> films not only overcome the temperature issue by operating at room temperature but also demonstrate high  $T_{\text{lum}}$  and large  $\Delta T_{\text{sol}}$  values in Fig. 5C, showing the unique advantages for practical smart window applications.

## DISCUSSION

In this study, we have achieved a reversible tristate phase transformation in a VO<sub>2</sub> epitaxial film by using solid electrolyte-assisted electric field control. These gating voltage-controlled phase transitions originate from the insertion/extraction of hydrogens into/from the VO<sub>2</sub> lattice. By changing the voltage, we can reversibly modulate the phase transformations among the insulating monoclinic VO<sub>2</sub>, the metallic H<sub>1-x</sub>VO<sub>2</sub> ( $0 < x < 1$ ), and the insulating HVO<sub>2</sub> phase structures. The transition between the metallic H<sub>x</sub>VO<sub>2</sub> phase and the insulating HVO<sub>2</sub> phase shows pronounced electrochromic effects at room temperature with greatly enhanced luminous transmittance in the visible range and the highest modulation efficiency in the NIR regions. This system overcomes the primary weaknesses of the traditional VO<sub>2</sub> smart window. Our findings thus demonstrate a facile route using phase modulation by a solid electrolyte for creating realistic energy-saving devices in the future.

## MATERIALS AND METHODS

### Thin-film growth

High-quality VO<sub>2</sub> (020) epitaxial films were grown on an Al<sub>2</sub>O<sub>3</sub> (0001) crystal substrate by radio frequency (rf) plasma-assisted oxide molecular beam epitaxy equipment; more details on film preparation were reported elsewhere (44).

### Solid electrolyte preparation

NaClO<sub>4</sub> (Sigma-Aldrich) dissolved in a PEO [molecular weight ( $M_w$ ) = 100,000; Sigma-Aldrich] matrix was used as the solid electrolyte. NaClO<sub>4</sub> and PEO powders (0.3 and 1 g, respectively) were mixed with 15 ml of anhydrous methanol (Alfa Aesar). The mixture was then stirred overnight at 50°C until a gel-like solid electrolyte was formed (45). A 10 mm by 10 mm electrolyte-covered VO<sub>2</sub> thin-film FET structure with three terminals was fabricated.

## Characterizations

Electrical properties were conducted by Keithley 2400 sourcemeters at room temperature. For the gating test, the voltage sweep rates were set to 1.0 V/2500 s for the fast mode and 1.0 V/10,000 s for the slow mode. Raman spectra (JY LabRAM HR, Ar+ laser at 514.5 nm, 0.5 mW) were recorded for different samples at room temperature. The laser spot size was 1 μm by 2 μm, and five points were tested for each film sample, which showed consistent results. The XPS (Thermo ESCALAB 250; Al K $\alpha$ , 1486.7 eV) was used to examine the chemical states of the VO<sub>2</sub> film samples before and after gating treatment. To detect the hydrogen concentration in the gated VO<sub>2</sub> film sample, SIMS measurements (Quad PHI 6600) were conducted.

XANES was conducted at the x-ray magnetic circular dichroism (XMCD) beamline (BL12B) at the National Synchrotron Radiation Laboratory (NSRL), Hefei. The NSRL is a second-generation accelerator with a 0.8-GeV storage ring, which is suitable for soft x-ray experiments. Total electron yield mode was applied to collect the sample drain current under a vacuum higher than  $3.0 \times 10^{-10}$  torr. The energy range is 100 to 1000 eV with an energy resolution ( $\Delta E/E$ ) of  $1.0 \times 10^{-3}$  at 1.0 keV, and the beam size is about 1.0 mm by 3.0 mm. High-resolution synchrotron XRD curves were characterized at the BL14B beamline of the Shanghai Synchrotron Radiation Facility (SSRF). The SSRF is a third-generation accelerator with a 3.5-GeV storage ring. The BL14B beamline shows an energy resolution ( $\Delta E/E$ ) of  $1.5 \times 10^{-4}$  at 10 keV and a beam size of 0.3 mm by 0.35 mm with a photon flux of up to  $2 \times 10^{12}$  phs/s at 10 keV. Considering the photon flux distribution and the resolution, the 0.124-nm x-ray was chosen for the experiment.

## First-principles calculations

All calculations were based on DFT, using the Vienna ab initio Simulation Package code (46). Exchange and correlation terms were described using general gradient approximation (GGA) in the scheme of Perdew-Burke-Ernzerhof (47). Core electrons were described by pseudopotentials generated from the projector-augmented wave method (48), and valence electrons were expanded in a plane-wave basis set with an energy cutoff of 480 eV. The GGA + U method was used to optimize the structure;  $U$  and  $J$  were chosen to be 4 and 0.68 eV, respectively. The relaxation was carried out until all forces on the free ions converged to 0.01 eV/Å. The climbing image nudged elastic band (49) method was used to find the minimum energy paths and the transition states for diffusion of H into VO<sub>2</sub> and H-doped VO<sub>2</sub>.

## SUPPLEMENTARY MATERIALS

Supplementary material for this article is available at <http://advances.sciencemag.org/cgi/content/full/5/3/eaav6815/DC1>

Fig. S1. Temperature-dependent gating-induced phase transitions.

Fig. S2. XPS spectra for the pure and gated VO<sub>2</sub> samples.

Fig. S3. SIMS test for the gated VO<sub>2</sub> film samples.

Fig. S4. Fourier transform infrared test for the residual methanol in PEO electrolyte.

Fig. S5. Stability test for the H-doped VO<sub>2</sub> films.

Fig. S6. Raman spectra for the films.

Fig. S7. Atomic structures of H<sub>x</sub>V<sub>4</sub>O<sub>8</sub>.

Table S1. Formation energies calculations.

Table S2. Comparison of the solar energy regulation ability ( $\Delta T_{\text{sol}}$ ) and luminous transmittance ( $T_{\text{lum}}$ ) values for various VO<sub>2</sub>-based smart-windows.

References (50–58)

## REFERENCES AND NOTES

1. T. Ramesh, R. Prakash, K. K. Shukla, Life cycle energy analysis of buildings: An overview. *Energy Build.* **42**, 1592–1600 (2010).
2. D. Bi, W. Tress, M. I. Dar, P. Gao, J. Luo, C. Renevier, K. Schenk, A. Abate, F. Giordano, J.-P. C. Baena, J.-D. Decoppet, S. M. Zakeeruddin, M. K. Nazeeruddin, M. Grätzel,

- A. Hagfeldt, Efficient luminescent solar cells based on tailored mixed-cation perovskites. *Sci. Adv.* **2**, e1501170 (2016).
3. C. Costa, I. Mesquita, L. Andrade, A. Mendes, Photoelectrochromic devices: Influence of device architecture and electrolyte composition. *Electrochim. Acta* **219**, 99–106 (2016).
  4. F. Bella, J. Popovic, A. Lamberti, E. Tresso, C. Gerbaldi, J. Maier, Interfacial effects in solid-liquid electrolytes for improved stability and performance of dye-sensitized solar cells. *ACS Appl. Mater. Interfaces* **9**, 3779–37803 (2017).
  5. M. Imperiyka, A. Ahmad, S. A. Hanifah, F. Bella, A UV-prepared linear polymer electrolyte membrane for dye-sensitized solar cells. *Physica. B Condens. Matter* **450**, 151–154 (2014).
  6. D. Pintoni, G. Iannaccone, A. Colombo, F. Bella, M. Välimäki, K.-L. Väisänen, J. Hast, M. Levi, C. Gerbaldi, C. Dragonetti, S. Turri, G. Griffini, Luminescent downshifting by photo-induced sol-gel hybrid coatings: Accessing multifunctionality on flexible organic photovoltaics via ambient temperature material processing. *Adv. Electron. Mater.* **2**, 1600288 (2016).
  7. S. Galliano, F. Bella, G. Piana, G. Giacoma, G. Viscardi, C. Gerbaldi, M. Grätzel, C. Barolo, Finely tuning electrolytes and photoanodes in aqueous solar cells by experimental design. *Sol. Energy* **163**, 251–255 (2018).
  8. R. Baetens, B. P. Jelle, A. Gustavsen, Properties, requirements and possibilities of smart windows for dynamic daylight and solar energy control in buildings: A state-of-the-art review. *Sol. Energy Mater. Sol. Cells* **94**, 87–105 (2010).
  9. R. M. Wentzcovitch, W. W. Schulz, P. B. Allen, VO<sub>2</sub>: Peierls or Mott-Hubbard? A view from band theory. *Phys. Rev. Lett.* **72**, 3389–3392 (1994).
  10. M. M. Qazilbash, M. Brehm, B.-G. Chae, P.-C. Ho, G. O. Andreev, B.-J. Kim, S. J. Yun, A. V. Balatsky, M. B. Maple, F. Keilmann, H.-T. Kim, D. N. Basov, Mott transition in VO<sub>2</sub> revealed by infrared spectroscopy and nano-imaging. *Science* **318**, 1750–1753 (2007).
  11. N. B. Aetukuri, A. X. Gray, M. Drouard, M. Cossale, L. Gao, A. H. Reid, R. Kukreja, H. Ohldag, C. A. Jenkins, E. Arenholz, K. P. Roche, H. A. Dürr, M. G. Samant, S. S. P. Parkin, Control of the metal-insulator transition in vanadium dioxide by modifying orbital occupancy. *Nat. Phys.* **9**, 661–666 (2013).
  12. H. Kim, Y. Kim, K. S. Kim, H. Y. Jeong, A.-R. Jang, S. H. Han, D. H. Yoon, K. S. Suh, H. S. Shin, T. Kim, W. S. Yang, Flexible thermochromic window based on hybridized VO<sub>2</sub>/graphene. *ACS Nano* **7**, 5769–5776 (2013).
  13. M. Li, S. Ji, J. Pan, H. Wu, L. Zhong, Q. Wang, F. Li, G. Li, Infrared response of self-heating VO<sub>2</sub> nanoparticles film based on Ag nanowires heater. *J. Mater. Chem. A* **2**, 20470–20473 (2014).
  14. M. Li, X. Wu, L. Li, Y. Wang, D. Li, J. Pan, S. Li, L. Sun, G. Li, Defect-mediated phase transition temperature of VO<sub>2</sub> (M) nanoparticles with excellent thermochromic performance and low threshold voltage. *J. Mater. Chem. A* **2**, 4520–4523 (2014).
  15. J. Zheng, S. Bao, P. Jin, TiO<sub>2</sub>(R)/VO<sub>2</sub>(M)/TiO<sub>2</sub>(A) multilayer film as smart window: Combination of energy-saving, antifogging and self-cleaning functions. *Nano Energy* **11**, 136–145 (2015).
  16. J. Zhu, A. Huang, H. Ma, Y. Ma, K. Tong, S. Ji, S. Bao, X. Cao, P. Jin, Composite film of vanadium dioxide nanoparticles and ionic liquid-nickel-chlorine complexes with excellent visible thermochromic performance. *ACS Appl. Mater. Interfaces* **8**, 29742–29748 (2016).
  17. M. Liu, B. Su, Y. V. Kaneti, Z. Chen, Y. Tang, Y. Yuan, Y. Gao, L. Jiang, X. Jiang, A. Yu, Dual-phase transformation: Spontaneous self-template surface-patterning strategy for ultra-transparent VO<sub>2</sub> solar modulating coatings. *ACS Nano* **11**, 407–415 (2017).
  18. T. Chang, X. Cao, N. Li, S. Long, X. Gao, L. R. Dedon, G. Sun, H. Luo, P. Jin, Facile and low-temperature fabrication of the thermochromic Cr<sub>2</sub>O<sub>3</sub>/VO<sub>2</sub> smart coatings: Enhanced solar modulation ability, high luminous transmittance and UV-shielding function. *ACS Appl. Mater. Interfaces* **9**, 26029–26037 (2017).
  19. Y. Chen, L. Fan, Q. Fang, W. Xu, S. Chen, G. Zan, H. Ren, L. Song, C. Zou, Free-standing SWNTs/VO<sub>2</sub>/Mica hierarchical films for high-performance thermochromic devices. *Nano Energy* **31**, 144–151 (2017).
  20. T. Chang, X. Cao, L. R. Dedon, S. Long, A. Huang, Z. Shao, N. Li, H. Luo, P. Jin, Optical design and stability study for ultrahigh-performance and long-lived vanadium dioxide-based thermochromic coatings. *Nano Energy* **44**, 256–264 (2018).
  21. Y. Wang, X. Sun, Z. Chen, Z. Cai, H. Zhou, T.-M. Lu, J. Shi, Defect-engineered epitaxial VO<sub>2-x</sub> in strain engineering of heterogeneous soft crystals. *Sci. Adv.* **4**, eaar3679 (2018).
  22. S.-Y. Li, G. A. Niklasson, C. G. Granqvist, Thermochromic fenestration with VO<sub>2</sub>-based materials: Three challenges and how they can be met. *Thin Solid Films* **520**, 3823–3828 (2012).
  23. M. Li, S. Magdassi, Y. Gao, Y. Long, Hydrothermal synthesis of VO<sub>2</sub> polymorphs: Advantages, challenges and prospects for the application of energy efficient smart windows. *Small* **13**, 1701147 (2017).
  24. S. Wang, M. Liu, L. Kong, Y. Long, X. Jiang, A. Yu, Recent progress in VO<sub>2</sub> smart coatings: Strategies to improve the thermochromic properties. *Prog. Mater. Sci.* **81**, 1–54 (2016).
  25. N. Lu, P. Zhang, Q. Zhang, R. Qiao, Q. He, H.-B. Li, Y. Wang, J. Guo, D. Zhang, Z. Duan, Z. Li, M. Wang, S. Yang, M. Yan, E. Arenholz, S. Zhou, W. Yang, L. Gu, C.-W. Nan, J. Wu, Y. Tokura, P. Yu, Electric-field control of tri-state phase transformation with a selective dual-ion switch. *Nature* **546**, 124–128 (2017).
  26. K. Liu, D. Fu, J. Cao, J. Suh, K. X. Wang, C. Cheng, D. F. Ogletree, H. Guo, S. Sengupta, A. Khan, C. W. Yeung, S. Salahuddin, M. M. Deshmukh, J. Wu, Dense electron system from gate-controlled surface metal-insulator transition. *Nano Lett.* **12**, 6272–6277 (2012).
  27. H. Ji, J. Wei, D. Natelson, Modulation of the electrical properties of VO<sub>2</sub> nanobeams using an ionic liquid as a gating medium. *Nano Lett.* **12**, 2988–2992 (2012).
  28. J. Jeong, N. Aetukuri, T. Graf, T. D. Schladt, M. G. Samant, S. S. P. Parkin, Suppression of metal-insulator transition in VO<sub>2</sub> by electric field-induced oxygen vacancy formation. *Science* **339**, 1402–1405 (2013).
  29. Y. Zhou, J. Park, J. Shi, M. Chhowalla, H. Park, D. A. Weitz, S. Ramanathan, Control of emergent properties at a correlated oxide interface with graphene. *Nano Lett.* **15**, 1627–1634 (2015).
  30. K. Shibuya, A. Sawa, Modulation of metal-insulator transition in VO<sub>2</sub> by electrolyte gating-induced protonation. *Adv. Electron. Mater.* **2**, 1500131 (2016).
  31. M. Nakano, D. Okuyama, K. Shibuya, M. Mizumaki, H. Ohsumi, M. Yoshida, M. Takata, M. Kawasaki, Y. Tokura, T. Arima, Y. Iwasa, Distinct substrate effect on the reversibility of the metal-insulator transitions in electrolyte-gated VO<sub>2</sub> thin films. *Adv. Electron. Mater.* **1**, 1500093 (2015).
  32. K. Sato, Y. Itoh, T. Aida, Columnar assembled liquid-crystalline peptidic macrocycles unidirectionally orientable over a large area by an electric field. *J. Am. Chem. Soc.* **133**, 13767–13769 (2011).
  33. Y. Filinchuk, N. A. Tumanov, V. Ban, H. Ji, J. Wei, M. W. Swift, A. H. Nevidomskyy, D. Natelson, In situ diffraction study of catalytic hydrogenation of VO<sub>2</sub>: Stable phases and origins of metallicity. *J. Am. Chem. Soc.* **136**, 8100–8109 (2014).
  34. J. Lin, H. Ji, M. W. Swift, W. J. Hardy, Z. Peng, X. Fan, A. H. Nevidomskyy, J. M. Tour, D. Natelson, Hydrogen diffusion and stabilization in single-crystal VO<sub>2</sub> micro/nanobeams by direct atomic hydrogenation. *Nano Lett.* **14**, 5445–5451 (2014).
  35. H. Yoon, M. Choi, T.-W. Lim, H. Kwon, K. Ihm, J. K. Kim, S.-Y. Choi, J. Son, Reversible phase modulation and hydrogen storage in multivalent VO<sub>2</sub> epitaxial thin films. *Nat. Mater.* **15**, 1113–1119 (2016).
  36. S. Chen, Z. Wang, L. Fan, Y. Chen, H. Ren, H. Ji, D. Natelson, Y. Huang, J. Jiang, C. Zou, Sequential insulator-metal-insulator phase transitions of VO<sub>2</sub> triggered by hydrogen doping. *Phys. Rev. B* **96**, 125130 (2017).
  37. Y. Chen, Z. Wang, S. Chen, H. Ren, L. Wang, G. Zhang, Y. Lu, J. Jiang, C. Zou, Y. Luo, Non-catalytic hydrogenation of VO<sub>2</sub> in acid solution. *Nat. Commun.* **9**, 818 (2018).
  38. J. Wei, H. Ji, W. Guo, A. H. Nevidomskyy, D. Natelson, Hydrogen stabilization of metallic vanadium dioxide in single-crystal nanobeams. *Nat. Nanotechnol.* **7**, 357–362 (2012).
  39. M. Abbate, The O 1s and sV 2p X-ray absorption spectra of vanadium oxides. *Brazilian J. Phys.* **24**, 785–795 (1994).
  40. R. Zimmermann, R. Claessen, F. Reinert, P. Steiner, S. Hüfner, Strong hybridization in vanadium oxides: Evidence from photoemission and absorption spectroscopy. *J. Phys. Condens. Matter* **10**, 5697 (1998).
  41. Y. Ke, C. Zhou, Y. Zhou, S. Wang, S. H. Chan, Y. Long, Emerging thermal-responsive materials and integrated techniques targeting the energy-efficient smart window application. *Adv. Funct. Mater.* **28**, 1800113 (2018).
  42. J. Lin, M. Lai, L. Dou, C. S. Kley, H. Chen, F. Peng, J. Sun, D. Lu, S. A. Hawks, C. Xie, F. Cui, A. P. Alivisatos, D. T. Limmer, P. Yang, Thermochromic halide perovskite solar cells. *Nat. Mater.* **17**, 261–267 (2018).
  43. A. Taylor, I. Parkin, N. Noor, C. Tummeltshammer, M. S. Brown, I. Papakonstantinou, A bioinspired solution for spectrally selective thermochromic VO<sub>2</sub> coated intelligent glazing. *Opt. Express* **21**, A750–A764 (2013).
  44. L. L. Fan, S. Chen, Y. F. Wu, F. H. Chen, W. S. Chu, X. Chen, C. W. Zou, Z. Y. Wu, Growth and phase transition characteristics of pure M-phase VO<sub>2</sub> epitaxial film prepared by oxide molecular beam epitaxy. *Appl. Phys. Lett.* **103**, 131914 (2013).
  45. Y. Yu, F. Yang, X. F. Lu, Y. J. Yan, Y.-H. Cho, L. Ma, X. Niu, S. Kim, Y.-W. Son, D. Feng, S. Li, S.-W. Cheong, X. H. Chen, Y. Zhang, Gate-tunable phase transitions in thin flakes of 1T-TaS<sub>2</sub>. *Nat. Nanotechnol.* **10**, 270–276 (2015).
  46. G. Kresse, D. Joubert, From ultrasoft pseudopotentials to the projector augmented-wave method. *Phys. Rev. B* **59**, 1758–1775 (1999).
  47. J. P. Perdew, K. Burke, M. Ernzerhof, Generalized gradient approximation made simple. *Phys. Rev. Lett.* **77**, 3865–3868 (1996).
  48. G. Kresse, J. Furthmüller, Efficient iterative schemes for ab initio total-energy calculations using a plane-wave basis set. *Phys. Rev. B* **54**, 11169–11186 (1996).
  49. D. Sheppard, P. Xiao, W. Chemelewski, D. D. Johnson, G. Henkelman, A generalized solid-state nudged elastic band method. *J. Chem. Phys.* **136**, 074103 (2012).
  50. Y. Choi, Y. Jung, H. Kim, Low-temperature deposition of thermochromic VO<sub>2</sub> thin films on glass substrates. *Thin Solid Films* **615**, 437–445 (2016).
  51. B. Zhu, H. Tao, X. Zhao, Effect of buffer layer on thermochromic performances of VO<sub>2</sub> films fabricated by magnetron sputtering. *Infrared Phys. Technol.* **75**, 22–25 (2016).
  52. M. Panagopoulou, E. Gagaoudakis, N. Boukos, E. Aperathitis, G. Kiriakidis, D. Tsoukalas, Y. S. Raptis, Thermochromic performance of Mg-doped VO<sub>2</sub> thin films on functional substrates for glazing applications. *Sol. Energy Mater. Sol. Cells* **157**, 1004–1010 (2016).

53. S. Long, H. Zhou, S. Bao, Y. Xin, X. Cao, P. Jin, Thermochromic multilayer films of  $\text{WO}_3/\text{VO}_2/\text{WO}_3$  sandwich structure with enhanced luminous transmittance and durability. *RSC Adv.* **6**, 106435–106442 (2016).
54. G. Sun, X. Cao, X. Gao, S. Long, M. Liang, P. Jin, Structure and enhanced thermochromic performance of low-temperature fabricated  $\text{VO}_2/\text{V}_2\text{O}_3$  thin film. *Appl. Phys. Lett.* **109**, 143903 (2016).
55. H. Liu, D. Wan, A. Ishaq, L. Chen, B. Guo, S. Shi, H. Luo, Y. Gao, Sputtering deposition of sandwich-structured  $\text{V}_2\text{O}_5/\text{metal (V, W)}/\text{V}_2\text{O}_5$  multilayers for the preparation of high-performance thermally sensitive  $\text{VO}_2$  thin films with selectivity of  $\text{VO}_2$  (B) and  $\text{VO}_2$  (M) polymorph. *ACS Appl. Mater. Interfaces* **8**, 7884–7890 (2016).
56. X. Wu, Z. Wu, H. Zhang, R. Niu, Q. He, C. Ji, J. Wang, Y. Jiang, Enhancement of  $\text{VO}_2$  thermochromic properties by Si doping. *Surf. Coatings Technol.* **276**, 248–253 (2015).
57. G. Sun, X. Cao, H. Zhou, S. Bao, P. Jin, A novel multifunctional thermochromic structure with skin comfort design for smart window application. *Sol. Energy Mater. Sol. Cells* **159**, 553–559 (2017).
58. E. Gagaoudakis, I. Kortidis, G. Michail, K. Tsagaraki, V. Binas, G. Kiriakidis, E. Aperathitis, Study of low temperature rf-sputtered Mg-doped vanadium dioxide thermochromic films deposited on low-emissivity substrates. *Thin Solid Films* **601**, 99–105 (2016).

#### Acknowledgments

**Funding:** This work was partially supported by the National Key Research and Development Program of China (2018YFA0208603, 2016YFA0401004), the National Natural Science Foundation of China (U1432249, 11404095, 11574279, and 11704362), the Fundamental

Research Funds for the Central Universities, the Youth Innovation Promotion Association CAS, the Major/Innovative Program of Development Foundation of Hefei Center for Physical Science and Technology, and the China Postdoctoral Science Foundation (2017M622002). This work was partially carried out at the USTC Center for Micro- and Nanoscale Research and Fabrication. We also acknowledge support from the XMCD beamline (BL12B), the photoelectron spectroscopy beamline (BL10B) at the NSRL (Hefei), and the x-ray diffraction beamline (BL14B1) at the SSRF. **Author contributions:** J.J. and C.Z. conceived the study. S.C. and C.Z. designed the experiments and performed the initial tests. Z.W. and J.J. conducted the theoretical calculations. S.C., H.R., Y.C., W.Y., C.W., and B.L. conducted the sample characterizations and synchrotron-based measurements. S.C., J.J., and C.Z. wrote the manuscript. All authors discussed the results and commented on the manuscript. **Competing interests:** The authors declare that they have no competing interests. **Data and materials availability:** All data needed to evaluate the conclusions in the paper are present in the paper and/or the Supplementary Materials. Additional data related to this paper may be requested from the authors.

Submitted 10 October 2018

Accepted 30 January 2019

Published 15 March 2019

10.1126/sciadv.aav6815

**Citation:** S. Chen, Z. Wang, H. Ren, Y. Chen, W. Yan, C. Wang, B. Li, J. Jiang, C. Zou, Gate-controlled  $\text{VO}_2$  phase transition for high-performance smart windows. *Sci. Adv.* **5**, eaav6815 (2019).

## Gate-controlled VO<sub>2</sub> phase transition for high-performance smart windows

Shi Chen, Zhaowu Wang, Hui Ren, Yuliang Chen, Wensheng Yan, Chengming Wang, Bowen Li, Jun Jiang and Chongwen Zou

*Sci Adv* 5 (3), eaav6815.  
DOI: 10.1126/sciadv.aav6815

ARTICLE TOOLS	<a href="http://advances.sciencemag.org/content/5/3/eaav6815">http://advances.sciencemag.org/content/5/3/eaav6815</a>
SUPPLEMENTARY MATERIALS	<a href="http://advances.sciencemag.org/content/suppl/2019/03/11/5.3.eaav6815.DC1">http://advances.sciencemag.org/content/suppl/2019/03/11/5.3.eaav6815.DC1</a>
REFERENCES	This article cites 58 articles, 4 of which you can access for free <a href="http://advances.sciencemag.org/content/5/3/eaav6815#BIBL">http://advances.sciencemag.org/content/5/3/eaav6815#BIBL</a>
PERMISSIONS	<a href="http://www.sciencemag.org/help/reprints-and-permissions">http://www.sciencemag.org/help/reprints-and-permissions</a>

Use of this article is subject to the [Terms of Service](#)

---

*Science Advances* (ISSN 2375-2548) is published by the American Association for the Advancement of Science, 1200 New York Avenue NW, Washington, DC 20005. 2017 © The Authors, some rights reserved; exclusive licensee American Association for the Advancement of Science. No claim to original U.S. Government Works. The title *Science Advances* is a registered trademark of AAAS.